TECHNICAL NOTE

Real-time trajectory guide tracking for intraoperative MRI-guided neurosurgery

Miles E. Olsen[1] │ **Ethan K. Brodsky[1]** │ **Jonathan A. Oler[2]** │ **Marissa K. Riedel[2]** │
Sascha A. L. Mueller[2] │ **Scott C. Vermilyea[3]** │ **Jeanette M. Metzger[3]** │
Yunlong Tao[4] │ **Kevin G. Brunner[3]** │ **Azam S. Ahmed[5]** │ **Su-Chun Zhang[4]** │
Marina E. Emborg[1,3] │ **Ned H. Kalin[2]** │ **Walter F. Block[1,6,7]**

[1]Department of Medical Physics, University of Wisconsin-Madison, Madison, Wisconsin USA

[2]Department of Psychiatry, University of Wisconsin–Madison, Madison, Wisconsin USA

[3]Wisconsin National Primate Research Center, University of Wisconsin-Madison, Madison, Wisconsin USA

[4]Waisman Center, University of Wisconsin-Madison, Madison, Wisconsin USA

[5]Department of Neurological Surgery, University of Wisconsin-Madison, Madison, Wisconsin USA

[6]Department of Biomedical Engineering, University of Wisconsin-Madison, Madison, Wisconsin USA

[7]Department of Radiology, University of Wisconsin-Madison, Madison, Wisconsin USA

Correspondence
Walter F. Block, Department Medical Physics, Institute University of Wisconsin-Madison, 1111 Highland Avenue Rm 1137, Madison, WI 53705, USA.
Email: wfblock@wisc.edu

Purpose: In current intraoperative MRI (IMRI) methods, an iterative approach is used to aim trajectory guides at intracerebral targets: image MR-visible features, determine current aim by fitting model to image, manipulate device, repeat. Infrequent updates are produced by such methods, compared to rapid optically tracked stereotaxy used in the operating room. Our goal was to develop a real-time interactive IMRI method for aiming.

Methods: The current trajectory was computed from two points along the guide's central axis, rather than by imaging the entire device. These points were determined by correlating one-dimensional spokes from a radial sequence with the known cross-sectional projection of the guide. The real-time platform RTHawk was utilized to control MR sequences and data acquisition. On-screen updates were viewed by the operator while simultaneously manipulating the guide to align it with the planned trajectory. Accuracy was quantitated in a phantom, and in vivo validation was demonstrated in nonhuman primates undergoing preclinical gene ($n = 5$) and cell ($n = 4$) delivery surgeries.

Results: Updates were produced at 5 Hz In 10 phantom experiments at a depth of 48 mm, the cannula tip was placed with radial error of (min, mean, max) = (0.16, 0.29, 0.68) mm. Successful in vivo delivery of payloads to all 14 targets was demonstrated across nine surgeries with depths of (min, mean, max) = (33.3, 37.9, 42.5) mm.

Conclusion: A real-time interactive update rate was achieved, reducing operator fatigue without compromising accuracy. Qualitative interpretation of images during aiming was rendered unnecessary by objectively computing device alignment.

KEYWORDS
cell delivery, gene delivery, intraoperative MRI, neurosurgery, nonhuman primates, real-time

---

1 | INTRODUCTION

When compared to stereotactic surgery in the operating room (OR), using only preoperative images, intraoperative MRI (IMRI) provides for increased control and accuracy by enabling imaging of target anatomy immediately prior to the aiming of an interventional device. Early IMRI efforts include the prospective stereotaxy technique introduced by Truwit,[1] illustrated in Figure 1A. The planned trajectory is formed by the anatomical target and the trajectory guide's pivot point. The line from target to pivot is extended to determine an "aim point" outside the body. Imaging is performed in the plane containing that aim point and is perpendicular to the planned trajectory. Alignment is achieved when the MR-visible stem is collinear with this trajectory (i.e. stem cross-section is centered on aim point). The stem is removed and a cannula introduced into the brain. An example of such an MR-compatible trajectory guide, the Food and Drug Administration-approved Navigus (Medtronic), is shown in Figure 1. This trajectory guide, used throughout the gene and cell delivery studies described herein, consists of a skull-mounted base containing a fixed (nontranslatable) ball joint that allows the trajectory to be oriented $\pm 18°$ off center.

A real-time interactive system for prospective stereotaxy was implemented by Martin et al.[2] with in-plane resolution of 1 mm and acquisition time of 200 ms. To accurately target small structures, higher spatial resolution imaging is needed which slows the rate of updates. Further developments by Brodsky et al.[3,4] improved in-plane resolution to 0.5 mm at the expense of acquisition time ($\approx$ 5 s/frame), and simplified the software development effort by building on the RTHawk[5] and Vurtigo[6] software packages.

Rather than image the entire device, trajectory determination can be accelerated by only acquiring a subset of one-dimensional (1D) MR readouts and exploiting a priori information about the trajectory guide's dimensions. We propose a method that uses a computational (rather than image-based) approach to provide real-time interactive feedback to the operator at 5 Hz, which is closer to the rate of optical tracking systems favored by neurosurgeons in the OR. We provide methodological details for implementation with a simple trajectory guide.[7] In addition to in vitro experiments, we present in vivo targeting results from nonhuman primate (NHP) subjects undergoing preclinical gene and cell delivery experiments with postoperative observation periods of months to years. We have applied the proposed method during our NHP work on cell delivery for Parkinson's disease[8-10] and viral vector gene delivery to study pathological anxiety.[11,12]

2 | METHODS

2.1 | Computational approach to real-time device tracking

The current trajectory of the guide can be tracked by obtaining two points along the central axis of the guide's cylindrical alignment stem. Exploiting the sparse object space, such points are readily computed by processing radial acquisitions from a plane intersecting the stem, as shown in Figure 1D–F. In practice, rather than perform 1D correlations in the image domain, each readout in the frequency domain is multiplied with the precomputed Fourier transform of the theoretical stem projection. That product is zero padded and inverse Fourier transformed to yield the interpolated correlation input to the peak finder. Multiple radial readouts are acquired with pulse repetition time on the order of 10–12 ms. Thus, by using 10–20 radial readouts, the system computes a new stem-plane intersection point every 100–200 ms. This process of computing the stem-plane intersection point is performed in two different offset planes, as shown in Figure 2C, to obtain a line representative of the current trajectory.

2.2 | Pivot point computation

The pivot must be identified correctly to calculate the correct aim point (Figure 2A). When the trajectory guide incorporates a fixed (nontranslatable) pivot point, after a precise one-time calculation of the pivot point, only one other point is needed to determine the trajectory.

The acquisition plane is prescribed based on an approximate pivot determined visually by the operator. The trajectory guide is then manipulated into multiple orientations (Figure 2B–D), yielding a collection of trajectory lines that are physically constrained to pass through the true pivot point at the ball joint center. These lines do not intersect exactly (due to noise, physical imperfection, etc.), but a linear least squares method computes their approximate intersection.[13] This computed pivot and a single real-time acquisition plane are then used for the final aiming step.

Glass NMR tubes (Wilmad-LabGlass) with 3 mm outer diameter and 10 cm length were used in place of the original alignment stems due to the NMR tubes' excellent physical cylindricity and low cost (Supporting Information Figure S1). We fabricated adapters (Supporting Information Figure S1C,D) to securely couple the NMR tube to the trajectory guide. All experiments were completed on a 3 T Discovery MR750 scanner (GE Healthcare), using a 10-cm single-channel loop coil (MR Instruments, Inc.).
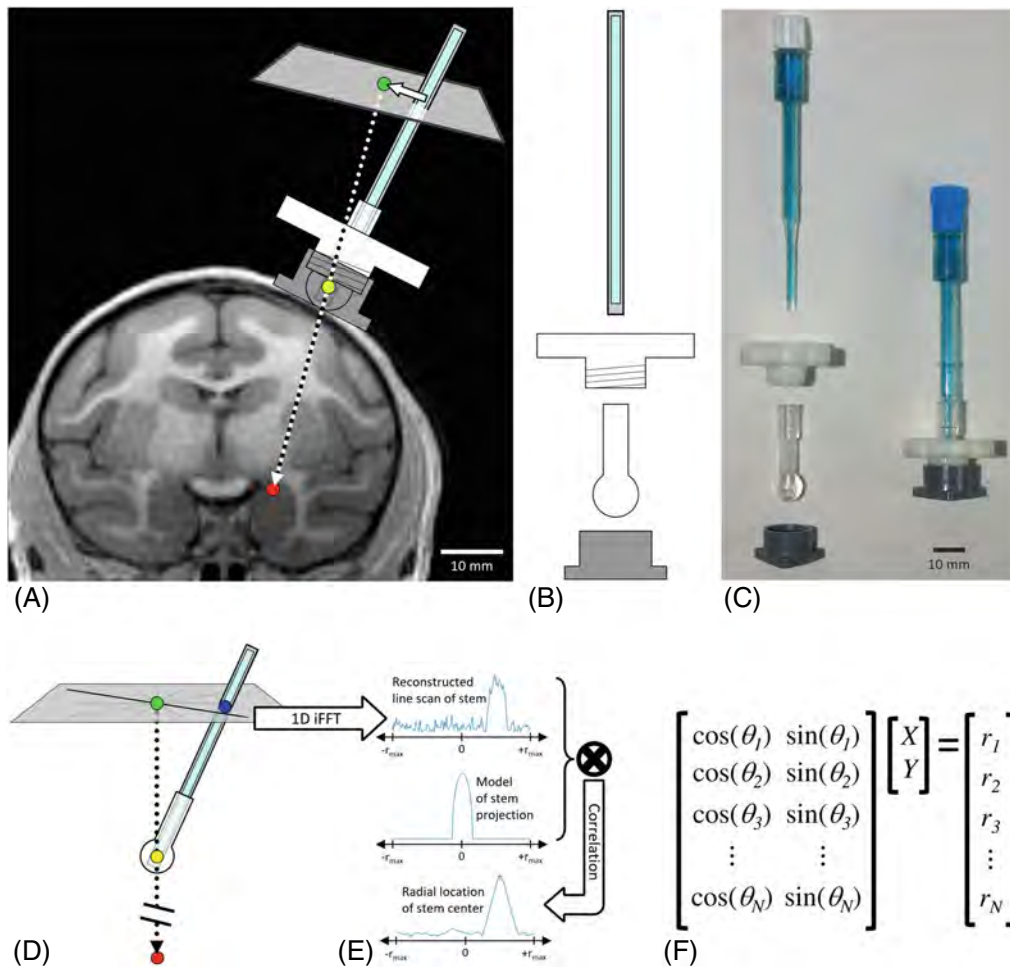
FIGURE 1 Prospective stereotaxy, trajectory guide, and computational tracking. (A) An aim point (green dot) is calculated by extending a line from the chosen target in the dorsal amygdala (red dot) out through the pivot point (yellow dot), which must be identified. The dotted arrow shows the planned trajectory, and the solid arrow indicates the manual adjustment needed to reorient the alignment stem along the planned trajectory. (B) The trajectory guide consists of (from bottom to top) a skull-mounted base, guide tube with pivoting ball joint, lock ring to immobilize ball joint, and an alignment stem filled with MR-visible fluid (light blue), as shown in this simplified exploded schematic and (C) photograph (exploded and assembled). The alignment stem intersects the acquisition plane (gray) at blue dot (D). The acquisition plane is prescribed perpendicular to the planned trajectory (dotted line). (E) Applying a one-dimensional inverse Fourier transform to a radial readout would reconstruct a line scan. Correlating the line scan with a model of the alignment stem projection enables a simple peak finder to detect the center location of the stem along each radial readout. In the proposed method, instead of doing a correlation in image space as depicted, it is accomplished via multiplication in the frequency domain. (F) The in-plane location of the stem center (X, Y) is calculated from the overdetermined system of equations arising from the MR readout angles (θ_i) and the detected peak radial locations (r_i) at those angles.

2.3 | In vitro testing

We performed in vitro targeting studies using a phantom to characterize the accuracy of pivot point computation and cannula tip placement.

2.3.1 | Pivot point computation

Precision was determined by performing 10 trials of computing the pivot as shown in Figure 2B–E. To ensure consistency of the true physical pivot, neither the patient table nor the phantom platform were moved. It would be ideal if these computed pivots could be compared to a known-true pivot location, but the true pivot is an infinitesimal point within a void at the center of the ball joint. Thus, the true pivot location can only be determined relative to some other MR-visible feature. The original Navigus hardware was designed to position the proximal tip of the alignment stem fluid at the true pivot, but we observe this to be imperfect. Therefore, accuracy of the computed pivots was determined indirectly by measuring the overall targeting accuracy of the entire guidance procedure.
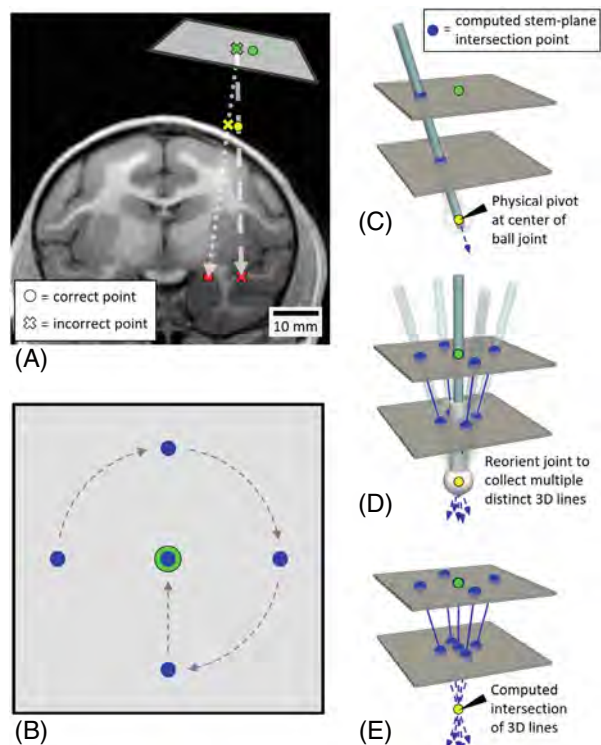
FIGURE 2 Computation of a refined pivot point. Manually selected pivot points are inherently imprecise, and error in the pivot point results in magnified error at target depth, as illustrated on preoperative MRI (A). For the dorsal amygdala target, (red dot) extrapolating out along dotted line through an incorrectly chosen pivot (yellow ✕) will result in an incorrect aim point (green ✕). The interventional device will pass through the true physical pivot point (yellow dot). If aligned with the aim point that is based on an incorrect pivot, it will follow the dashed line trajectory, placing the tip at an incorrect target (red ✕). (B) Illustration of operator's view of acquisition plane, showing aim point (green) and a progression (dashed arrows) of five stem-plane intersection points (blue dots) as the ball joint is reoriented. (C) Computing stem-plane intersection points (blue dots) at two positions along the stem's length yields a line (blue arrow) representing the current trajectory. (D) The distinct trajectory guide orientations are recorded, and since all trajectories are physically constrained to pass through the pivot point (the center of the trajectory guide's ball joint), computing the intersection of those three-dimensional lines yields that pivot point (E).

2.3.2 | Targeting accuracy

Accuracy was measured across 10 trials of guiding the cannula tip to a target (Figure 3C) consisting of a cylinder machined down to an outer diameter of 1 mm. The target was placed securely inside a small, fluid-filled box ($55 \times 55 \times 75$ mm^3) which has a Navigus trajectory guide base on its lid (Figure 3D). The box was clamped in a wide, 7.5 kg acrylic platform to prevent the box from moving.

The guidance procedure began with identifying the MR coordinates of the target spike on a roadmap scan produced by a three-dimensional (3D) T1-weighted, Cartesian gradient-recalled echo sequence with inversion recovery preparation, a $256 \times 224 \times 124$ acquisition matrix ($0.7 \times 0.8 \times 0.8$ mm^3 voxels) in a coronal slab, TE 3.9 ms, pulse repetition time 9.1 ms, TI 450 ms, and flip angle of 12° with a scan time of 6 min 4 s (hereafter referred to as the 3D T$_1$W sequence).

The pivot point was manually identified on the roadmap, then refined using the pivot point computation procedure above. With the target and pivot (red and yellow dots, respectively, in Figure 1A), our software calculated the aim point (green dot, Figure 1A) at an operator-selected offset from the pivot. In the experiments presented here, the real-time MR device tracking provided five updates per second displayed on a monitor visible to the operator as they aimed the trajectory guide.

Once aimed, the MR-visible alignment stem was removed and replaced by the remote introducer, a precise linear stage (Medtronic) for moving the cannula to the target depth. Our software calculated the planned insertion depth using the pivot point, target point, and the offset between the cannula tip and the physical pivot point when the depth gauge on the remote introducer is zeroed. Finally, the remote introducer was used to advance the cannula to the planned insertion depth. After insertion, the 3D T$_1$W sequence was repeated to validate the cannula tip location.

To measure the final cannula tip location, the postinsertion 3D T$_1$W volumes were opened in 3D Slicer[14,15] and the three view planes were reformatted such that the cannula laid in the peri-sagittal and peri-coronal planes, and passed perpendicularly through the peri-axial plane. The 3-mm section of shaft-tip overlap (illustrated in Figure 3B) creates the darkest negative contrast, with fainter contrast in the shaft above it, and even fainter contrast in the 3 mm tip below it, as seen on MRI in Figure 3F. Slicer's ruler tools were used to measure these two 3-mm-long features to corroborate the cannula tip location, which was then recorded. Retrospective determination of cannula tip placement using reformatted slices[16] and comparing MRI-visible features to measured cannula dimensions[17] has been previously described.

2.4 | In vivo applications

The proposed guidance method was applied in studies requiring precise cannula placement in NHP models: (1) convection-enhanced delivery of viral vectors to a subregion of the amygdala, intended to alter anxious temperament in five rhesus macaques (3 male, age at surgery = 2.19 ± 0.23 years)[12] and (2) delivery of engineered cells to the substantia nigra to test cell-based dopamine replacement for
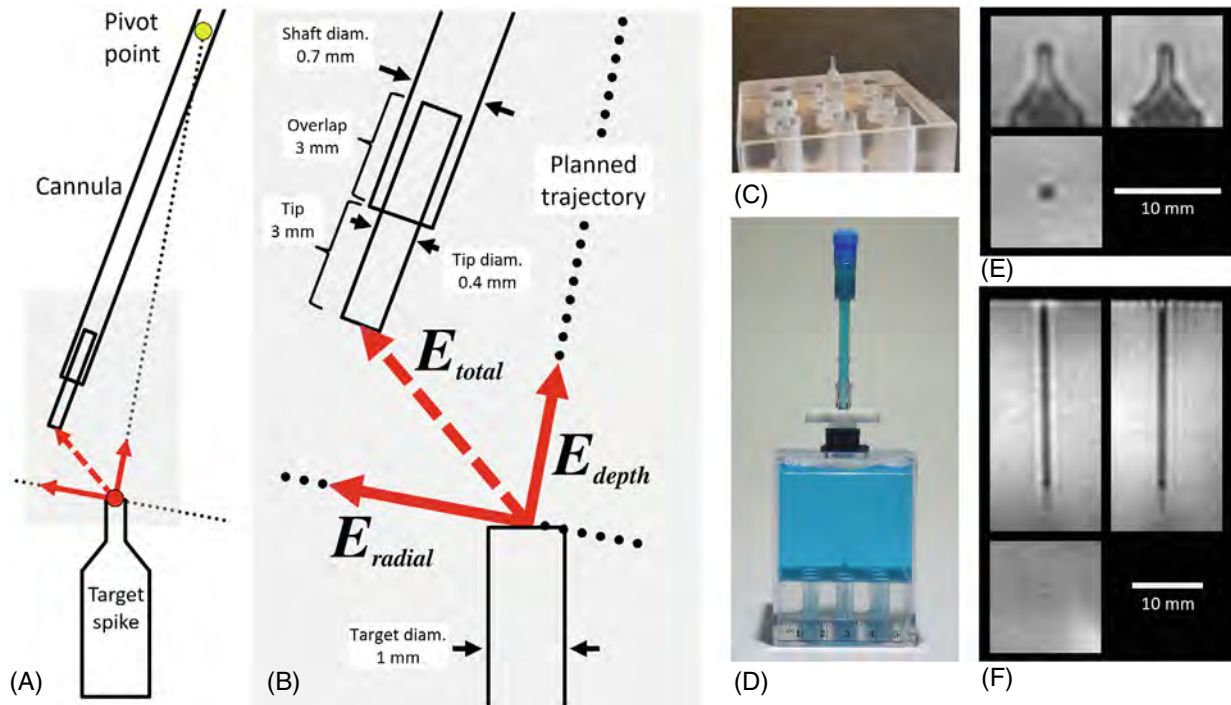
FIGURE 3 Determination of tip placement error. A simplified illustration shows a two-dimensional view of the target spike, cannula, and tip placement three-dimensional (3D) error vectors (red arrows) used in the phantom study of accuracy (A). The planned trajectory passes through the pivot point, down to the target spike. That trajectory line and its perpendicular plane are indicated with dotted black lines. A close-up view (B) of the gray box in (A) shows the depth and radial error vectors (solid red arrows) obtained by projecting the total 3D error vector (dashed red arrow) onto the trajectory vector, and the perpendicular plane, respectively. A close-up photo (C) of the target spike in the central position of the array block and a photo of the array block inside the precision testing box with a trajectory guide attached to the lid (D) illustrate the size and shape of the target. 3D T1-weighted inversion recovery MRI volumes are used to identify the target point before aiming, as well as the cannula tip after insertion. The target point at the tip of the spike is identified by viewing oblique slices aligned with the target tip (E), and similarly, the cannula tip location is identified by viewing oblique slices aligned with the cannula (F). The cannula tip location is visually determined by the presence of darker negative contrast in the 3-mm overlap section, and fainter negative contrast in the 3-mm tip.

Parkinson's disease in four rhesus macaques with 1-methyl-4-phenyl-1,2,3,6-tetrahydropyridine-induced hemiparkinsonism (four male, age at surgery = 15.31 ± 5.85 years). The surgical procedure and equipment are described in our previous work,[18] as are the in vivo positron emission tomography and postmortem histology methods that were used to show successful implantation of similar cells after delivery to the putamen using this IMRI method.[9] The experiments were performed according to the federal guidelines on animal use and care[19] with approval of University of Wisconsin–Madison Institutional Animal Care and Use Committees.

3 | RESULTS

3.1 | Pivot point computation

3.1.1 | In vitro experiments

The proposed method allows us to repeatedly compute pivot points, observing variation well below 0.1 mm (smaller than the voxel dimensions of the 3D T_1W scan used for planning). The repeatability of pivot point computation in vitro is visualized by plotting the demeaned point cloud in Figure 4A,B. In the radial plane, Bessel's corrected sample SD $s = 0.03$ mm, with no point deviating from the mean by more than 0.05 mm. Along the depth direction, $s = 0.05$ mm, with no point deviating from the mean by more than 0.08 mm. For these trajectory guides, it is expected that depth variation will be greater than radial (Figure S2).

3.1.2 | In vivo experiments

The discrepancies between manual and computed pivots in vivo are shown in Figure 4F,G. Taking the computed pivot to be representative of the true physical pivot, a greater discrepancy indicates greater error in the manually selected pivot coordinates. Across the nine in vivo experiments, the cannula tip was successfully placed at all 14 targets. For 12 targets, the planned aim was achieved
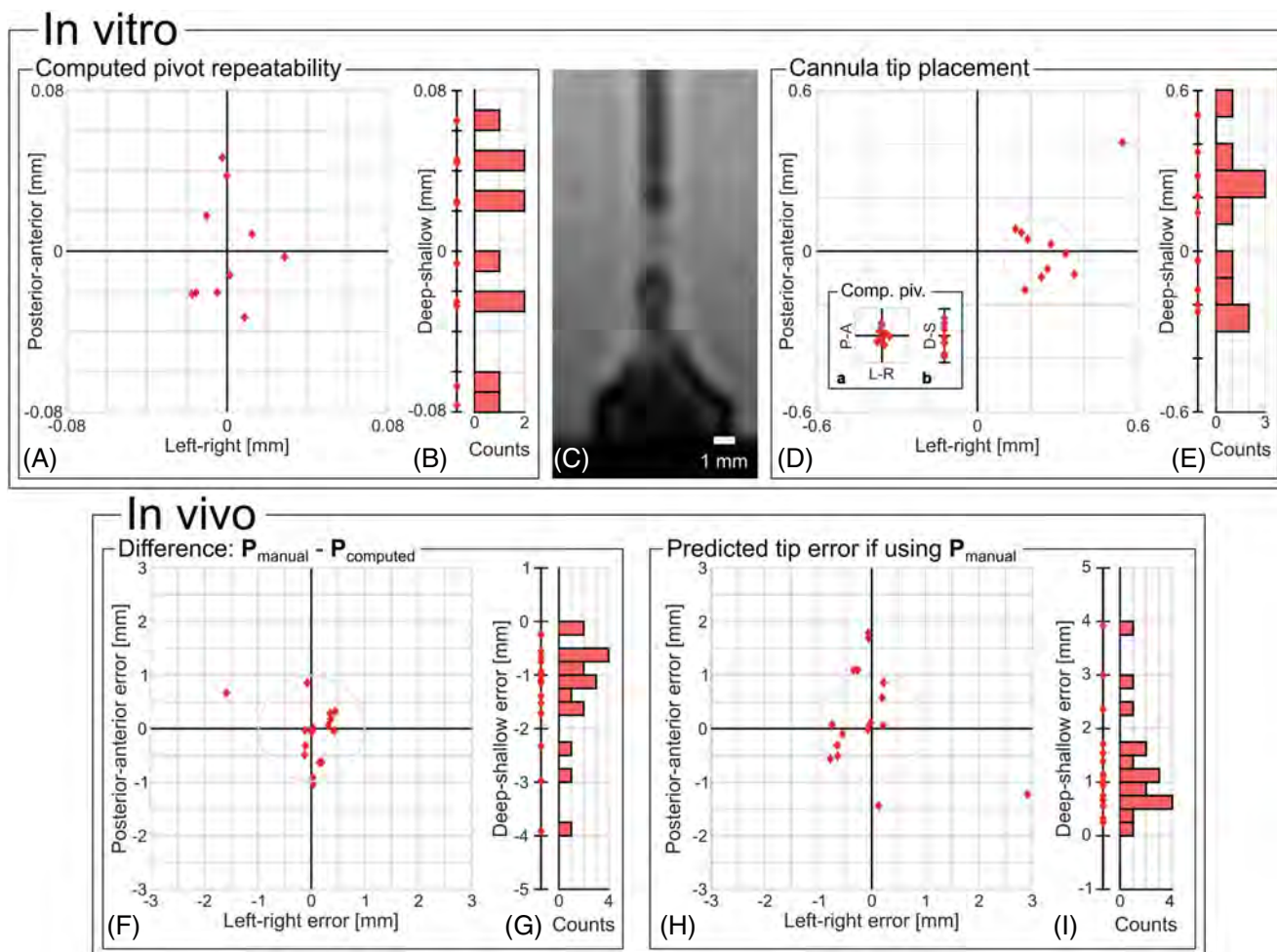
FIGURE 4 In vitro and in vivo precision and accuracy. The repeatability of the computed pivot is shown by plotting the demeaned point cloud from 10 independent trials of pivot computation (A, B). (A) The two-dimensional scatter shows the radial variation of the computed pivot points and (B) the one-dimensional scatter and histogram show the variation along the depth direction. In vitro cannula tip placement is shown in C–E. (C) 3D T_1W MRI of the cannula after insertion toward the 1-mm diameter spike target. (D) Radial and (E) depth error of the cannula tip after aiming at the spike target and inserting, exhibiting a small bias to the right of the target. The first trial had the greatest radial error and the subsequent nine are more tightly grouped, falling within a circle (gray) of radius 0.14 mm at target depth of 48.3 mm. Expressed as an angular measure that is independent of target depth, those nine trajectories are within 2.9 mrad of the circle center. Inset within (D) shows the data from (A, B), resized to match the scale of (D, E) for comparison, emphasizing that the computed pivots are more tightly clustered than the cannula tip locations. In vivo results over 17 instances of pivot computation show how the manually selected pivot ($\mathbf{P}_{manual}$) differs from the computed pivot ($\mathbf{P}_{computed}$, at origin) for each trial in the (F) radial and (G) depth directions. The gray circle (r = 1 mm) shows that two manual pivots had > 1 mm of radial error with respect to the computed pivot. In all cases, the manually selected pivot was deeper than the computed pivot. To illustrate the importance of correctly determining the pivot, the predicted (H) radial and (I) depth error in tip placement is modeled under the assumptions that (1) the computed pivot is the true physical pivot, but (2) the trajectory guide is aimed based on the manual pivot, then (3) a cannula inserted with no deflection. If the pivot refinement procedure had been omitted, the six trials outside the gray circle were predicted to result in > 1 mm radial error with respect to the target.

and the cannula inserted after the first round of aiming. The remaining two targets required six rounds of aiming before insertion due to the following issues during four rounds: resetting the head holder; swapping out a slippery ball joint that would not lock; target anatomy shifting 1.2 mm deeper into bore, likely due to subject or scanner table being bumped, possibly during monitoring of

vitals; and the 3D T_1W aim confirmation scan predicting ≈ 1.1 mm lateral error (the experimental protocol entailed re-aiming if predicted lateral error > 1 mm). One round of aiming was performed without computing a pivot, using the manually selected pivot, for a total of 17 computed pivots. Examining the 17 instances of pivot computation (Figure 4F,G), the manually identified approximate pivots
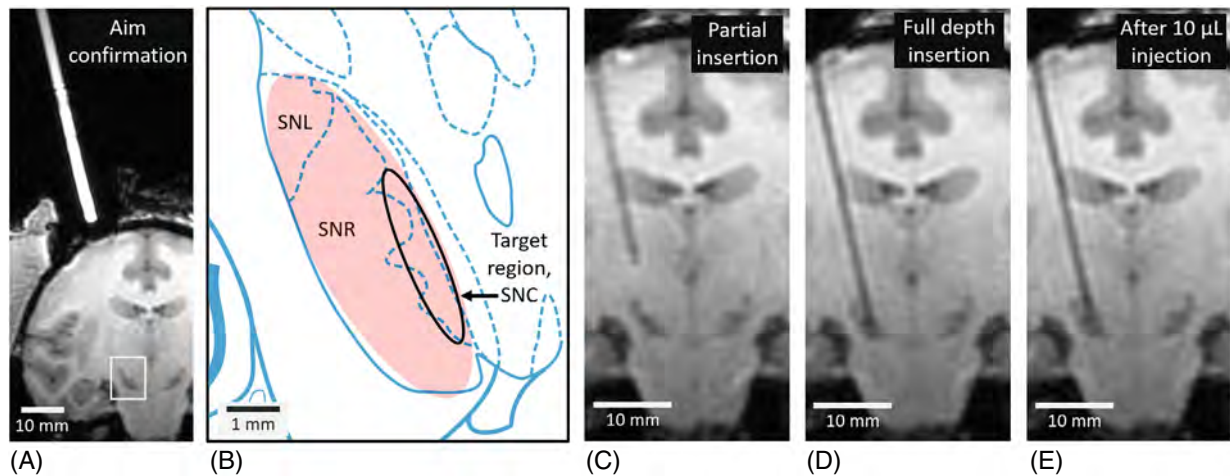
FIGURE 5 Visualization of cell delivery process. An aim confirmation scan (T1-weighted, cerebrospinal fluid-nulling IR) is acquired after aiming and locking the trajectory guide. A peri-coronal view from an oblique slice through the middle of the stem (A) allows the operator to verify, before inserting the cannula, that the alignment stem and target location in the substantia nigra (SN) are indeed collinear. An anatomical atlas illustration of the SN subregions (B) approximately corresponds to the white box area in (A). The SN is highlighted in red and the intended treatment region (black oval) corresponds to the SN pars compacta (SNC) subregion, which is medial to the larger pars reticulata (SNR) and lateral (SNL) subregions. Adapted with permission from Paxinos et al. rhesus atlas,[24] figure 69. Another MRI volume is acquired after the cannula is inserted to a partial depth (C). The cannula's negative contrast against the brain parenchyma allows the operator to determine the current position of the tip and measure the remaining distance to the target. After advancing the remaining 8 mm to this target, another three-dimensional volume (D) is acquired to verify that the cannula tip has been successfully placed in the thin, obliquely oriented SNC target. A final MRI volume (E) is acquired after injecting cells suspended in artificial cerebrospinal fluid. Two 5 μl deposits were injected, with the cannula retracted 1 mm between deposits.

differ from the computed pivots in the radial direction by 0.53 ± 0.43 mm (mean$\pm$ SD), with a maximum deviation of 1.71 mm.

3.2 | Targeting results

3.2.1 | In vitro experiments

Figure 4C–E shows targeting results from 10 attempts to place the cannula tip on a 1.0 mm cylindrical target at a depth of 48.3 mm from the pivot. The first trial shows the greatest radial error, < 0.7 mm, which is still less than the voxel size of the 3D T^1W scan used for intraoperative planning and monitoring. The subsequent nine trials are more tightly clustered together, with the greatest radial error in that group being < 0.4 mm. No depth error exceeded 0.6 mm. Expressed in angular units, which are independent of depth, the radial error of the first trial is 14 mrad, and the subsequent group of nine has error ranging from 3.4 to 7.7 mrad.

3.2.2 | In vivo experiments

Postmortem verification of the infusate delivery, transfection by the viral vector, and subsequent expression of

delivered genes is demonstrated by the in vivo positron emission tomography and histology imaging in our previous work.[12]

Cells were injected unilaterally in the substantia nigra (SN) of four NHP subjects. Peri-coronal views show the aligned trajectory guide and targeted SN prior to cannula insertion (Figure 5A), after partial insertion (Figure 5C), and after full insertion and deposit of the cells (Figure 5D,E). In the 3D T_1W validation scan, due to the artificial cerebrospinal fluid in which the cells were suspended, the inversion recovery sequence yields negative contrast in the region where the cells were delivered. Subjects were maintained for 1.37 ± 0.30 years (mean $\pm$ SD) of observation before necropsy. Analysis of positron emission tomography, histology, and parkinsonism symptoms will be reported elsewhere.

4 | DISCUSSION

In this work, a computational tracking method was developed for aiming neurosurgical trajectory guides in conventional diagnostic MRI scanners, and the method was validated in vitro and in vivo. Rather than imaging the entire device and fitting a 3D model of the trajectory guide to the image volume, the proposed method uses a priori information about the hardware and a small set of

MR measurements to rapidly track the current trajectory. After a one-time computation of the non-translatable pivot point, the system presents the operator with real-time interactive feedback as they aim at the planned target.

The proposed method has been successfully applied to achieve submillimeter accuracy in preclinical procedures including gene and cell delivery. The proposed IMRI method enables researchers to monitor the infusate delivery and verify that the intended target was successfully treated. Without IMRI, such verification would not typically be achieved until postmortem histological assessment of the brain tissue.

4.1 | Applicability to other trajectory guides

We expect that the proposed method could be applied to other trajectory guides that have a linear MR-visible feature indicative of the current trajectory. The ball-joint guide array[20] is similar to the Navigus and the version with MR contrast along its central axis[21] should work with this method. For trajectory guides that have both translational and rotational degrees of freedom such as the SmartFrame[22] or GantryMate,[16] this method would require two acquisition planes along the trajectory guide fiducial, with a proportionally slower update rate.

4.2 | Predicted tip error

Radial error is more important to minimize than depth error, as excessive radial error may result in missing the target, while depth error (if shallow) can be corrected by advancing. If the refined pivot had not been computed and the trajectory guide had been aimed based only on the manually selected pivot (with our typical aiming offset of 50 mm), the radial error of the inserted cannula tip would be expected to range from 0.07 to 3.13 mm, with mean radial error of 0.95 mm (Figure 4H). More generally, the radial errors can be expressed in angular units that are independent of depth. Predicted radial error would range from 1.8 to 75.5 mrad, with mean of 26.2 mrad. For reference, at a target depth of 40 mm (typical in our NHP experiments), a 1-mm radial error is an angular error of 25 mrad.

4.3 | Benefits of this method

This method provides rapid and accurate alignment, objective determination of the pivot and stem-plane intersection points, and increased update rate.

4.3.1 | Tip placement accuracy

Our in vitro tip placement accuracy compares favorably to our previous image-based work,[18] and is similar to that reported for commercial systems in humans.[17,23] Our radial errors of (min, mean, max) = (3.4, 6.1, 14.0) mrad are comparable to the radial errors of cannula tip placement recently achieved by another lab, (0.7, 6.2, 17.2) mrad, using a mechanically similar trajectory guide across 22 insertions in humans.[21] However, the numbers are not entirely comparable as those human experiments had an average insertion depth of 137 mm. Compared to water, which offers little resistance, it is harder to maintain precision over long depths in the brain where the cannula could be deflected slightly by tissue along the way, or brain shift could affect the target position. Ignoring the first-trial outlier, our radial error is evenly distributed along the anterior-posterior axis, but the mean of that group is biased 0.24 mm (4.9 mrad) right of the target. This systematic error is smaller than the voxel size of the 3D T_1W scan used during IMRI, and we plan to identify the cause and correct it. Experiments by another lab using a similar trajectory guide have also observed a small bias in their mean cannula tip placement across 15 insertions in NHPs.[20]

4.3.2 | Increased update rate

The proposed method reduces the operator fatigue experienced during our previous image-based real-time method, which required waiting for 5 s between image updates to see the result of aiming movement.

The success of the proposed method is supported by the quantification of accuracy in experiments with a rigid phantom, and by the precise insertion of cannulae into neurosurgical targets in over 71 surgeries in NHPs,[8-12] to be quantified and discussed in a future publication.

4.4 | Limitations

This technique is still preliminary and has not yet undergone human-scale testing. Mapping MR signal to spatial location has inherent error due to inhomogeneity of B_0 and tissue, and especially gradient nonlinearity which worsens with distance from isocenter. These issues affect the 3D T_1W volumes and real-time tracking to some unknown degree. Therefore, the observed angular error is not entirely comparable to similar procedures in humans with greater target depth. Careful testing in human-mimicking

phantoms or cadavers is warranted before translating this technique to humans.

This method assumes the use of a trajectory guide with a fixed (nontranslatable) pivot point. In order to detect inadvertent motion (e.g. table or head frame translation), a rapid two-dimensional confirmatory imaging sequence could improve time efficiency relative to the slow 3D T_1W confirmation scan used here. Furthermore, surgeons may prefer a guide like the ClearPoint SmartFrame that also supports translation. Tracking such a guide necessitates two acquisition planes, at least doubling the update latency.

This method requires that the scanner support real-time control and acquisition processing, which may not be available on all systems. While the aiming step is faster, considerable time is still spent at the MRI during these procedures (see timeline in Figure S3).

5 | CONCLUSIONS

We have proposed a method for rapid trajectory guide tracking and demonstrated its successful application in phantoms and neurosurgeries on NHPs. The approach provides real-time feedback on device orientation at an interactive rate (5 Hz) which, compared to fully sampled IMRI techniques, is closer to that of the rapid tracking enjoyed by neurosurgeons in stereotactic operating rooms.

The data presented here emphasize the value of real-time MR guidance and intraoperative MRI validation of the spatial distribution of experimental therapies in animal models, as compared to the limitations of stereotactic surgery without MRI.

CONFLICT OF INTEREST
Olsen, Brodsky, and Block are co-inventors on a patent for this technique. The patent (recently approved by USPTO) has been transferred to the Wisconsin Alumni Research Foundation (WARF).

ORCID
Miles E. Olsen https://orcid.org/0000-0002-3569-1732
Jonathan A. Oler https://orcid.org/0000-0002-1333-6924
Walter F. Block https://orcid.org/0000-0002-2262-9972

TWITTER
Walter F. Block @Bucky_Block

REFERENCES
1. Truwit CL, Liu H. Prospective stereotaxy: a novel method of trajectory alignment using real-time image guidance. *J Magn Reson Imaging*. 2001;13:452-457.
2. Martin AJ, Larson PS, Ostrem JL, et al. Placement of deep brain stimulator electrodes using real-time high-field interventional magnetic resonance imaging. *Magn Reson Med*. 2005;54:1107-1114.
3. Brodsky EK, Block WF, Alexander AL, Emborg ME, Ross CD, Sillay KA. Intraoperative device targeting using real-time MRI. In: Proceedings of the 2011 Biomedical Sciences and Engineering Conference: Image Informatics and Analytics in Biomedicine; 2011:1-4; Knoxville, TN. http://ieeexplore.ieee.org/document/5872335/
4. Brodsky EK, Olsen ME, Oler JA, et al. MRI-guided delivery of viral vectors for targeted alteration of neurochemistry. Proceedings of the 8th National Image-Guided Therapy Workshop; 2016:28; Bethesda, Maryland.
5. Santos JM, Wright GA, Pauly JM. Flexible real-time magnetic resonance imaging framework. Proceedings of the 26th Annual International Conference of the IEEE Engineering in Medicine and Biology Society; Vol. 3; 2004:1048-1051; IEEE, San Francisco. http://ieeexplore.ieee.org/document/1403343/

6. Pintilie S, Biswas L, Anderson K, Dick S, Wright G, Radau P. Visualization software for real-time, image-guided therapeutics in cardiovascular interventions. Proceedings of the CI2BM09-MICCAI Workshop on Cardiovascular Interventional Imaging and Biophysical Modelling; 2009: 141-148.

7. Hall WA, Liu H, Truwit CL. Navigus trajectory guide. *Neurosurgery*. 2000;46:502-504. https://academic.oup.com/neurosurgery/article/46/2/502/2931566

8. Vermilyea SC, Lu J, Olsen M, et al. Real-time intraoperative MRI intracerebral delivery of induced pluripotent stem cell-derived neurons. *Cell Transpl*. 2017;26: 613-624.

9. Zammit M, Tao Y, Olsen ME, et al. [18F]FEPPA PET imaging for monitoring CD68-positive microglia/macrophage neuroinflammation in nonhuman primates. *EJNMMI Res*. 2020;10:93. https://ejnmmires.springeropen.com/articles/10.1186/s13550-020-00683-5

10. Tao Y, Vermilyea SC, Zammit M, et al. Autologous transplant therapy alleviates motor and depressive behaviors in parkinsonian monkeys. *Nat Med*. 2021. http://www.nature.com/articles/s41591-021-01257-1

11. Fox AS, Souaiaia T, Oler JA, et al. Dorsal amygdala neurotrophin-3 decreases anxious temperament in primates. *Biol Psych*. 2019;86:881-889. https://linkinghub.elsevier.com/retrieve/pii/S0006322319314878

12. Roseboom PH, Mueller SAL, Oler JA, et al. Evidence in primates supporting the use of chemogenetics for the treatment of human refractory neuropsychiatric disorders. *Mol Therapy*. 2021;S1525001621002094. https://linkinghub.elsevier.com/retrieve/pii/S1525001621002094

13. user1551, point closest to a set four of lines in 3D; 2011. Online. Accessed 24 February 2021. https://math.stackexchange.com/a/55286

14. Fedorov A, Beichel R, Kalpathy-Cramer J, et al. 3D slicer as an image computing platform for the quantitative imaging network. *Magnet Reson Imaging*. 2012;30:1323-1341. https://linkinghub.elsevier.com/retrieve/pii/S0730725X12001816

15. Kikinis R, Pieper SD, Vosburgh KG. 3D slicer: a platform for subject-specific image analysis, visualization, and clinical support. In: Jolesz FA, ed. *Intraoperative Imaging and Image-Guided Therapy*. Springer; 2014:277-289.

16. Reichert A, Bock M, Vogele M, Krafft AJ. GantryMate: a modular MR-compatible assistance system for MR-guided needle interventions. *Tomography*. 2019;5:266-273. https://www.mdpi.com/2379-139X/5/2/00007

17. Chittiboina P, Heiss JD, Lonser RR. Accuracy of direct magnetic resonance imaging-guided placement of drug infusion cannulae. *J Neurosurg*. 2015;122:1173-1179. https://thejns.org/view/journals/j-neurosurg/122/5/article-p1173.xml

18. Emborg ME, Joers V, Fisher R, et al. Intraoperative intracerebral MRI-guided navigation for accurate targeting in nonhuman primates. *Cell Transpl*. 2010;19: 1587-1597.

19. Clark JD, Gebhart GF, Gonder JC, Keeling ME, Kohn DF. The 1996 guide for the care and use of laboratory animals. *ILAR J*. 1997;38:41-48.

20. Sudhakar V, Mahmoodi A, Bringas JR, et al. Development of a novel frameless skull-mounted ball-joint guide array for use in image-guided neurosurgery. *J Neurosurg*. 2020; 132:595-604. https://thejns.org/view/journals/j-neurosurg/132/2/article-p595.xml

21. Bankiewicz KS, Pasterski T, Kreatsoulas D, et al. Use of a novel ball-joint guide array for magnetic resonance imaging–guided cannula placement and convective delivery: technical note. *J Neurosurg*. 2020;1-7.

22. Richardson RM, Kells AP, Martin AJ, et al. Novel platform for MRI-guided convection-enhanced delivery of therapeutics: preclinical validation in nonhuman primate brain. *Stereotact Funct Neurosurg*. 2011;89:141-151. https://www.karger.com/Article/FullText/323544

23. Larson PS, Starr PA, Bates G, Tansey L, Richardson RM, Martin AJ. An optimized system for interventional magnetic resonance imaging-guided stereotactic surgery: preliminary evaluation of targeting accuracy. *Oper Neurosurg*. 2012;70:ons95-ons103. https://academic.oup.com/ons/article/70/suppl_1/ons95/2408667

24. Paxinos G, Petrides M, Huang XF, Toga AW. *The Rhesus Monkey Brain: in Stereotaxic Coordinates*. 2nd ed. Elsevier, Acad. Press; 2009 OCLCL:845195997.

SUPPORTING INFORMATION

Additional supporting information may be found in the online version of the article at the publisher's website.

Figure S1. Timeline of in vivo procedures. To give an idea of where time is spent during our NHP in vivo IMRI surgeries, this table shows the various steps and time to perform them. In surgeries with only a single delivery (such as those targeting the substantia nigra in this work), the procedure ends after the first removal of the cannula. For the typical case of multiple targets, the procedure continues beyond the bottom row the table, restarting at "Interpret roadmap volume", until all targets have been treated. Figure S2. Geometric explanation of error distribution in pivot computation. A simplified two-dimensional illustration explaining why the computed pivot repeatability experiment shows more depth variation than radial variation. Comparing (A) and (B): for a given angular separation (e.g., 30°) between the trajectories, using (A) offsets of 10 and 50 mm will more tightly bound the worst-case computed pivot than (B) offsets of 20 and 40 mm. Comparing (B) and (C): for given offsets, if the trajectories are (C) perpendicular, the worst-case computed pivot is more tightly bound than if the trajectories are (b) closer to parallel. Hence, we use near and far offsets (usually 10 and 50 mm), and orient the trajectory guide at its extreme range of motion limits when computing the current trajectory during the pivot computation step. Figure S3. Timeline of in vivo procedures. To give an idea of where time is spent during our NHP in vivo IMRI surgeries, this table shows the various steps and time to perform them. In surgeries with only a single delivery (such as those targeting the substantia nigra in this work), the procedure ends after the

first removal of the cannula. For the typical case of multiple targets, the procedure continues beyond the bottom row the table, restarting at "Interpret roadmap volume", until all targets have been treated.